Desalination and Water Treatment
www.deswater.com

doi: 10.5004/dwt.2022.28307

253 (2022) 239–247
March

High-efficiency ternary Ag/C@Bi_2MoO_6 photocatalyst: electron transformation, 2,4-dibromophenol degradation and mechanism

Mingyang Liu[a], Ningbo Sun[b], Dong Ma[a,*]

[a]*College of Resource and Environment, Qingdao Agricultural University, No. 700 Changcheng Road, Qingdao 266109, China, emails: dma796@hotmail.com (D. Ma), liumingyang626@outlook.com (M. Liu)*
[b]*Human Resources Department, Qingdao Agricultural University, 700 Changcheng Road, Qingdao 266109, China, email: nbsun@qau.edu.cn (N. Sun)*

Received 13 September 2021; Accepted 3 February 2022

ABSTRACT

A novel Ag nanoparticle modified and carbon layer coated bismuth molybdate (Ag/C@Bi_2MoO_6) composite was successfully synthesized by hydrothermal and ultrasonic methods to attain a high-efficiency route for both reductive dehalogenation and oxidative decomposition of halogenated organics (e.g., 2,4-dibromophenol, 2,4-DBP). The carbon layer was tightly combined with Bi_2MoO_6 by C–O–Bi or C–O–Mo bonds, and the coated carbon layer provided a rapid electron transformation route by its excellent conductivity to enhance the separation of photoexcited charges on the surface of Bi_2MoO_6 according to the transmission emission microscopy, Fourier-transform infrared spectroscopy, X-ray photoelectron spectroscopy, and photoluminescence characterizations. The Ag nanoparticles were deposited via the ultrasonic method and built an electric field to aggregate much more electrons on their surface and separate further photoexcited charges from the photoluminescence results. The 2,4-DBP is efficiently degraded by the Ag/C@Bi_2MoO_6 composite under visible-light irradiation, and the 0.5% Ag/C@Bi_2MoO_6 composite demonstrated an extremely removal efficiency of 2,4-DBP (10 mg/L) of 87% within 180 min. The degradation process is started with debromination process in the conduction band by aggregating electrons and followed by the oxidization and mineralization processed in valence band by holes and •OH radicals. This study displays a new approach for halophenols degradation by the heterogeneous photocatalytic process.

Keywords: Visible-light photocatalyst; Bismuth molybdate (Bi_2MoO_6); Carbon layer; Ag; 2,4-dibromophenol

1. Introduction

Halophenols such as 2,4-dibromophenol (2,4-DBP) occurred at high concentrations in freshwater systems, soils, and sediments in the recent decades around the world [1,2]. Advanced oxidation processes (AOPs) technology has been regarded as an important method to degrade and mineralize halophenol contaminants [3,4]. Visible-light induced photocatalytic technology is widely used due to the almost complete mineralization and the low cost with renewable sunlight [5–8]. Bismuth molybdate (Bi_2MoO_6), one of the bismuth contained semiconductor compounds, has attracted a great deal of attention due to the excellent photosensitivity and high photocatalytic activity under visible-light irradiation. Bi_2MoO_6 consists of $[Bi_2O_2]^{2+}$ layers sandwiched between MoO_4^{2-} sheets and has a band gap energy of 2.2~2.5 eV which is in good agreement with the sunlight spectrum [9,10].

It is well known that the low separation efficiency of photoexcited charge carriers affects the photocatalytic performance of semiconductor photocatalyst [11]. Researchers have tried various methods to improve the photocatalytic

* Corresponding author.

activity of Bi_2MoO_6, including noble metal deposition, metal ion doping, and semiconductor composites [12–14]. Recently, much attention has been paid to the photocatalyst coating with carbon, which can stabilize the catalyst surface and increase the photocatalytic activity. Chen et al. [15] have successfully synthesized carbon-coated $ZnIn_2S_4$ nanocomposites and found that the carbon coating significantly increases the photocatalytic efficiency and photostability of RhB degradation. In the previous work, we have prepared a carbon-coated Bi_2MoO_6 to enhance the separation efficiency of photoexcited electrons and by using low-cost glucose precursors [16,17]. The coated carbon layer on the surface could apply a rapid transmission route for electrons to inhibit the combination of charges and improve photocatalytic activity.

However, the utilization of electrons transmitting from the surface of the photocatalyst is another challenge to improve the charge separation. Noble metals such as gold (Au), silver (Ag), palladium (Pd), and platinum (Pt) could be used as electron traps near the conduction band to facilitate carrier transfer and prevent recombination with valence band holes [18–22]. At the same time, the electric field could be formed by the plasmonic effect of noble metal atoms and accelerate the aggregation of the transmitting electrons. Among all the noble metals, Ag has attracted the great interest of researchers because of its ability to handle organic pollutants over other noble metals and their additional antimicrobial activity [23,24]. Therefore, we conclude that the separated electrons would have a rapid route to an acceptor made up of Ag particles.

In this study, carbon-coated Bi_2MoO_6 (C@Bi_2MoO_6) was prepared by the addition of glucose as a precursor hydrothermal method. We are confident that the coated carbon layer would show great contract between the carbon and Bi_2MoO_6 rather than graphene and CNT in our previous study [2,8]. Then Ag deposited C@Bi_2MoO_6 (Ag/C@Bi_2MoO_6) composite was synthesized by an ultrasonic deposition method. The as-prepared Ag/C@Bi_2MoO_6 composite significantly improves the photocatalytic activity under visible-light irradiation. This is mainly attributed to the synergistic effect of noble metal (Ag) and coated carbon layer on the surface of Bi_2MoO_6, which enhances the separation efficiency of photogenerated electron-hole pairs and improves the photocatalytic activity.

2. Experimental

2.1. Synthesis of Bi_2MoO_6

All reagents for synthesis and analysis were analytic grade without further purification, and deionized water was used throughout the experiments. The Bi_2MoO_6 photocatalyst was synthesized via a common method of hydrothermal technique. In a typical procedure, 2.0 mmol $Bi(NO_3)_3{\cdot}5H_2O$ was dissolved into 10 mL dilute HNO_3 (2 mol/L) (solution A). Secondly, 2.0 mmol $(NH_4)_6Mo_7O_{24}{\cdot}4H_2O$ was dissolved into 60 mL of deionized water at 70°C (solution B). Solution A was dropped into solution B with stirring and reacted for 60 min and the pH of the suspension was adjusted to 7.0 using $NH_3{\cdot}H_2O$. The resulting mixture was sealed into a 100 mL Teflon-lined stainless steel autoclave and heated at 180°C for 12 h. The products of Bi_2MoO_6 were collected by filtration, washed with deionized water several times, and dried by vacuum at 80°C for 8 h.

2.2. Synthesis of C@Bi_2MoO_6 composites

0.1 g Bi_2MoO_6 was added to 80 mL glucose solution (30 mg/L) with stirring for 30 min, and the mixture solution was sealed into a 100 mL Teflon-lined stainless steel autoclave and heated at 180°C for 6 h. The products of C@Bi_2MoO_6 composites were collected by filtration, washed with deionized water, and dried by vacuum at 80°C for 8 h.

2.3. Synthesis of Ag/C@Bi_2MoO_6 composites

Ag/C@Bi_2MoO_6 composites were synthesized by an ultrasonic method. Typically, 2.5 mL $NaBH_4$ (0.1 mol/L), 0.2 g as-obtained C@Bi_2MoO_6 composites, and a certain amount of $AgNO_3$ were added to 100 mL deionized water, and then ultrasonicated for 30 min. The mixture solution was filtrated and dried to obtain the Ag/C@Bi_2MoO_6 composites. The different deposition amount of Ag to Ag/C@Bi_2MoO_6 was controlled to be 0.25%, 0.50%, 1.00%, and 2.00%.

2.4. Characterization

The crystalline phases of the samples were evaluated by X-ray powder diffraction (XRD) on a Bruker D8 Advance diffract meter (Bruker, Germany). The diffraction patterns were determined in the 2θ range of 10°–80° with a Cu Kα source (λ = 1.5418 Å) running at 60 kV and 60 mA. The morphologies and microstructures of the samples were obtained by a scanning electron microscope (SEM, JEOL 7500F) combined with an energy dispersive X-ray spectrometer (EDX) and a high-resolution transmission emission microscopy (HR-TEM, JEOL, JEM 2100). The infrared spectra were examined by a Fourier-transform infrared spectrometer (FTIR, Nicolet Avatar 370). X-ray photoelectron spectroscopy (XPS) measurements were examined via an ESCALAB 250 spectrometer (Thermo Fisher Scientific, UK) with non-monochromatic Al Kα X-rays (1486.6 eV). UV-VIS diffuse reflectance spectra (DRS) were characterized by a UV-VIS spectrophotometer (TU-1901) with $BaSO_4$ as a reference. The photoluminescence (PL) spectra of the photocatalysts were examined by a fluorescence spectrometer (Hitachi F-4600) with an excitation wavelength of 365 nm.

2.5. Photocatalytic activity

The photocatalytic activities of the samples were evaluated by 2,4-DBP degradation with a visible-light source (λ > 420 nm, 500 W Xe lamp) due to its high occupancy of the sunlight. The as-prepared photocatalyst (0.1 g) was dispersed into 100 mL of 2,4-DBP solution (10 mg/L of 2,4-DBP concentration). Before visible-light irradiation, the mixture was magnetically stirred in the dark for 30 min to reach the equilibrium of adsorption and desorption. The solutions were collected at different time intervals and centrifuged to remove the particles. The obtained solution was analyzed through high-performance liquid chromatography (HPLC) at 280 nm to determine 2,4-DBP concentration.

To capture the corresponding active species, various sacrificial agents were added into the 2,4-DBP solution. $Na_2C_2O_4$ (5 mmol/L), Cr (VI) (0.5 mmol/L), IPA (5 mmol/L), and TEMPOL (2 mmol/L) were employed as the scavengers to capture hole, electron, hydroxyl radical (•OH) and superoxide radical ($•O_2^-$), respectively.

3. Results and discussion

3.1. Crystalline structure and morphology

The as-prepared Bi_2MoO_6 photocatalyst is identical to orthorhombic according to the XRD patterns (Fig. 1), and the main diffraction peaks of composites were identical to the orthorhombic phase (JCPDS No. 76-2388) [25,26]. The peaks of carbon are not observed in XRD patterns of the $C@Bi_2MoO_6$ and $Ag/C@Bi_2MoO_6$ composites, indicating that the amorphous carbon is present in these composites. The significant peaks of Ag were hardly observed in the XRD patterns of composites, and it suggests that Ag has a high dispersion and low concentration in the composites [27]. The intensities of the diffraction peaks of Bi_2MoO_6 are gradually weaker by increasing the deposition of Ag, indicating that Ag deposition affects the crystalline structure of Bi_2MoO_6 photocatalyst.

The $Ag/C@Bi_2MoO_6$ composite is composed of irregular sheets with a thickness of about a hundred nanometers, which is the bulk of Bi_2MoO_6 in the composite, as shown in Fig. 2a. The EDX spectrum of the 0.50% $Ag/C@Bi_2MoO_6$ composite linked to SEM in Fig. 2b shows that C and Ag elements are coated in the surface of the composite. To further confirm the existence of carbon and Ag, the elemental mapping image of the 0.50% $Ag/C@Bi_2MoO_6$ composite was measured and is shown in Fig. 2c1–c4. The C, Bi, Mo, and Ag elements are uniformly distributed on the surface of the composite. It suggests that the C layer generated by the hydrothermal method is very thin, and the Ag nanoparticles dispersed more tenuously than C on the surface of the composite. Ag nanoparticles have a diameter of about 10~20 nm and are grown on the surface of the composite, which can be seen in TEM images as shown in Fig. 3a and b. The distinct lattice fringes of d = 0.204 nm and 0.236 nm in the high-resolution TEM image in Fig. 3c match with the crystallographic planes of Ag (200) and (111), respectively [28]. Also, the lattice fringes of d = 0.316 nm are found and assigned to the (131)

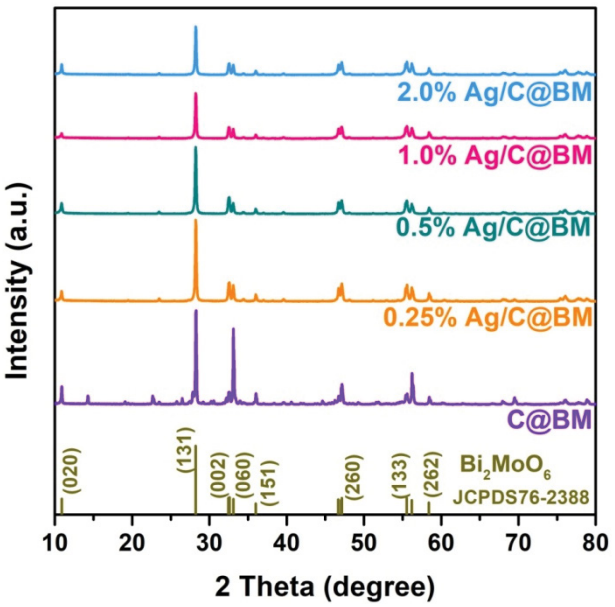

Fig. 1. XRD patterns of the $C@Bi_2MoO_6$ and $Ag/C@Bi_2MoO_6$ composites.

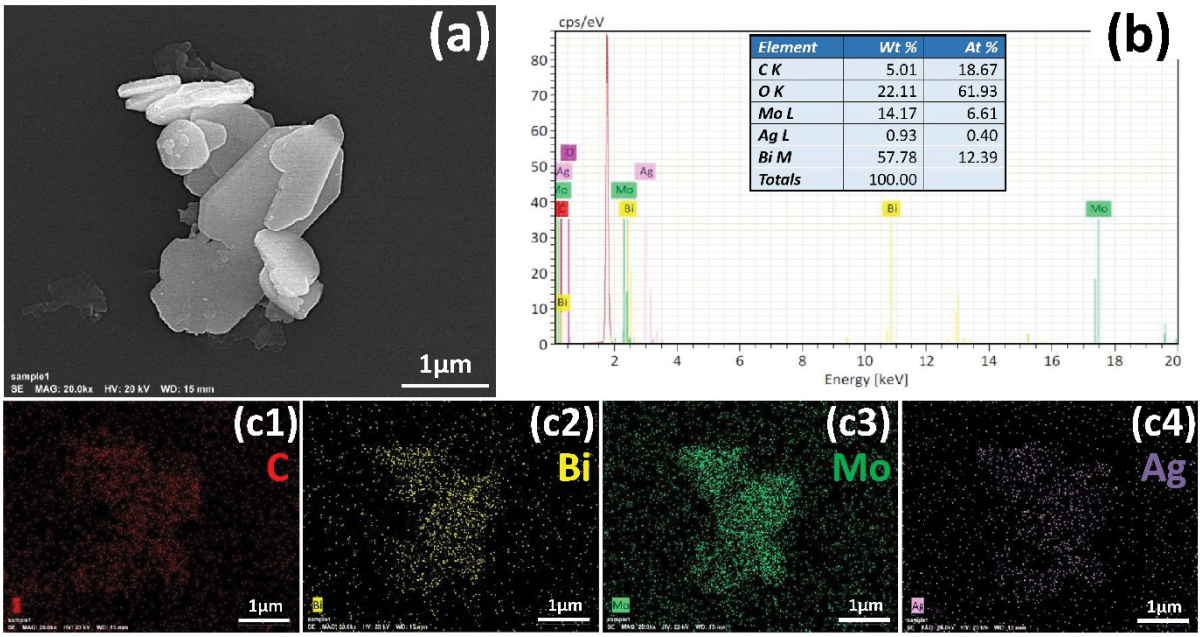

Fig. 2. SEM (a), EDX (b) and elemental mapping images (c) of the 0.50% $Ag/C@Bi_2MoO_6$, (c1) C, (c2) Bi, (c3) Mo and (c4) Ag elements.

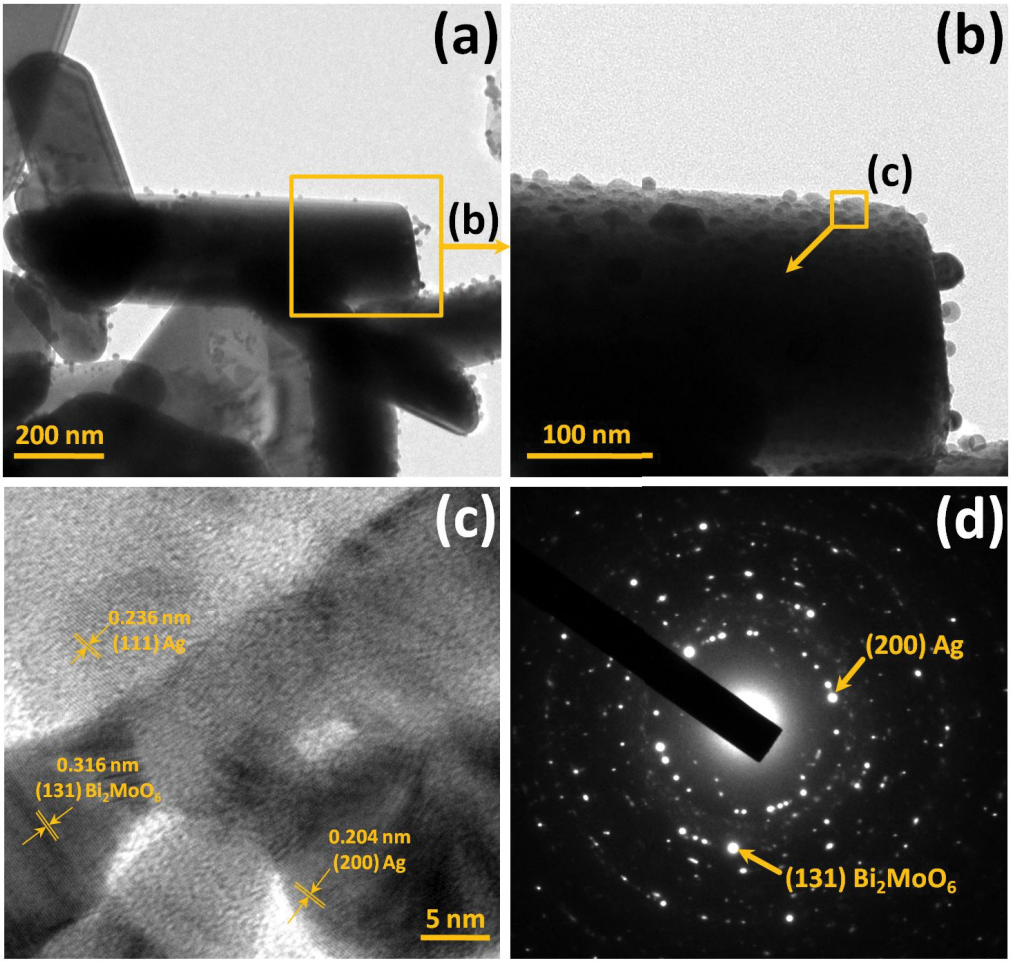

Fig. 3. TEM (a, b), HR-TEM (c) images and SAED pattern (d) of the 0.50% Ag/C@Bi_2MoO_6 composite.

plane in the orthorhombic phase of Bi_2MoO_6. However, we cannot observe the carbon layer on the outer edge of the Bi_2MoO_6 sheets due to the layer is too thin to confirm. In the SAED pattern of the 0.50% Ag/C@Bi_2MoO_6 composite, as shown in Fig. 3d, the crystallographic planes of Ag (200) and Bi_2MoO_6 (111) have also appeared.

3.2. Surface structure and photoexcited properties

The surface element chemical composition of the photocatalyst is investigated by XPS spectra. The survey XPS spectrum of 0.5% Ag/C@Bi_2MoO_6 composite is shown in Fig. 4a, and we can find the C 1s and Ag 3d peaks (inset) in the composite. The obtained high-resolution spectrum for Mo 3d is shown in Fig. 4b, and the peaks at 235.2 and 232.0 eV are related to Mo $3d_{3/2}$ and Mo $3d_{5/2}$ of MoO_4^{2-} in Bi_2MoO_6 photocatalyst, respectively. The obtained high-resolution C 1s spectrum is shown in Fig. 4c, and the asymmetric peak around 282~288 eV could be fitted to four peaks at 287.0, 284.9, 283.6, and 283.2 eV. The peaks at 287.0 eV and 283.2 eV correspond to the C=O bond and the C=C bond, respectively [29]. The peak at 283.6 eV corresponds to the C–C bond in the surface of the 0.5% Ag/C@Bi_2MoO_6 composite. The peak at 284.9 eV corresponds to Mo–O–C bond and the Bi–O–C bond formed between Bi_2MoO_6 and the carbon layer. It indicates that there is a formation of the Metal–O–C bond between carbon and $[Bi_2O_2]^{2+}$ structure in the 0.5% Ag/C@Bi_2MoO_6 composite [30]. As indicated in Fig. 4d, the asymmetric peak around 527~532 eV of O 1s could be fitted to four peaks at about 529.9, 528.8, 528.3, and 531.4 eV. The peaks at 529.9 and 528.8 eV correspond to the C=O bond and Mo–O bond in 0.5% Ag/C@Bi_2MoO_6 composite, respectively. The peaks at 528.3 and 531.4 eV correspond to Mo–O–C bond and the Bi–O–C bond, respectively [17]. The obtained high-resolution spectrum of Ag 3d is shown in Fig. 4e. The peaks at 372.5 and 366.4 eV are related to Ag $3d_{3/2}$ and Ag $3d_{5/2}$ of Ag in composite, respectively. The interval between the two peaks is 6.1 eV, which confirms that Ag exists in a metal state, but Ag cannot be detected by XRD due to its high dispersion [31]. Generally, the carbon layer can tightly bind to Bi_2MoO_6 with the formation of C–O–Bi and C–O–Mo bonds on the surface of the composite, and Ag^0 is the major chemical state of Ag nanoparticles.

FTIR analysis is also an important method to reveal the surface structure of photocatalyst materials. Fig. 4f shows the FTIR spectra of Bi_2MoO_6, C@Bi_2MoO_6, and 0.5% Ag/C@Bi_2MoO_6 composites. The bands at 400~900 cm^{-1} are appeared

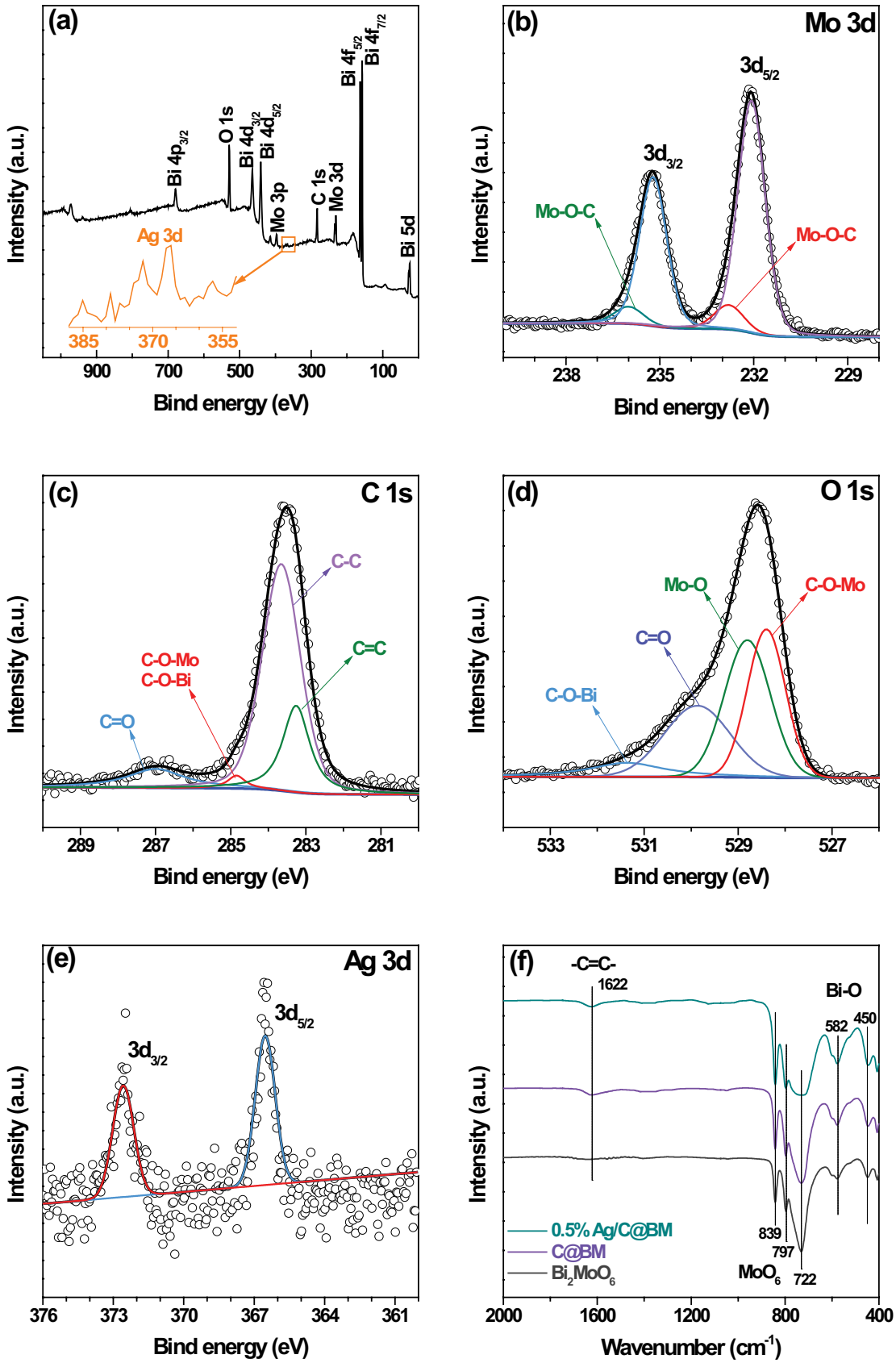

Fig. 4. Survey XPS spectrum (a) and high-resolution XPS spectra of the 0.5% Ag/C@Bi_2MoO_6 (BM) composite with Mo 3d (b), C 1s (c), O 1s (d) and Ag 3d (e), and FTIR spectra (f) of pure Bi_2MoO_6, C@BM and 0.5% Ag/C@BM composite.

in the samples, corresponding to the Bi–O, Mo–O stretching, and Mo–O–Mo bridging stretching modes. The bands at 450 and 582 cm^{-1} are attributed to Bi–O deformation vibration and stretching vibration, respectively. The bands at around 722 and 839 cm^{-1} are assigned to the asymmetric stretching mode of MoO_6 involving vibrations of the equatorial and apical oxygen atoms, respectively. The bands at 797 cm^{-1} can be attributed to the stretching mode of MoO_6 involving vibrations of the apical oxygen atoms [32]. The band at 1,622 cm^{-1} is assigned to the vibration mode of C=C, and the peaks can be found in the spectra of $C@Bi_2MoO_6$ and 0.5% $Ag/C@Bi_2MoO_6$ composites, indicating the existence of a carbon layer on the surface of the composite.

Bi_2MoO_6 is a visible light excitable photocatalyst, and the absorption edge at about 480 nm, as shown in the UV-Vis DRS curve in Fig. 5a. The visible light absorption intensity of $C@Bi_2MoO_6$ and 0.5% $Ag/C@Bi_2MoO_6$ composites are enhanced after carbon layer coating and Ag nanoparticles deposition. It reveals that the introductions of both carbon and Ag have significant effects on increasing the visible light absorption and thus narrowing the bandgap [17].

The PL analysis was carried out to explore the migration, transfer, and recombination of photogenerated electrons and holes of the as-prepared samples. The PL emission at about 470 nm is a feature near edge emission, which is more conducive to the recombination of photoexcited electrons and holes [33]. The PL emission intensity of the 0.5% $Ag/C@Bi_2MoO_6$ composite, as shown in Fig. 5b, decreases remarkably compared with the pure Bi_2MoO_6 and $C@Bi_2MoO_6$, suggesting that the recombination of photoexcited electrons and holes was blocked with the deposition of Ag nanoparticles. Therefore, the enhanced separation of photoexcited electrons and holes would is favorable for the quantum efficiency of the 0.5% $Ag/C@Bi_2MoO_6$ composite, and improve its photocatalytic activity.

3.3. Photocatalytic activities and mechanism

The photocatalytic degradation curves of pure Bi_2MoO_6, $C@Bi_2MoO_6$, and $Ag/C@Bi_2MoO_6$ composites during 2,4-DBP degradation under visible light irradiation is shown in Fig. 6a. In dark conditions, $C@Bi_2MoO_6$ and $Ag/C@Bi_2MoO_6$ composites showed similar adsorption properties, suggesting that Ag deposition could hardly improve the textural properties (The BET surface areas of $C@Bi_2MoO_6$ and $Ag/C@Bi_2MoO_6$ composites are 5.56 m^2/g [16] and 5.92 m^2/g, respectively). The 2,4-DBP has little degradation in photolysis under visible-light irradiation, but its concentration has a remarkable decrease with the addition of $C@Bi_2MoO_6$ and $Ag/C@Bi_2MoO_6$ photocatalysts. Compared with the $C@Bi_2MoO_6$, Ag deposition on the surface of the $C@Bi_2MoO_6$ photocatalyst can enhance the photocatalytic activity of the composite, and the 2,4-DBP removal rate reaches 87% within 180 min under visible-light irradiation over 0.5% $Ag/C@Bi_2MoO_6$ composite, showing a high performance according to previous research [34]. It demonstrates that 0.5% of the Ag deposition amount is the best one and too less or too many Ag deposition would reduce the photocatalytic activity of the $Ag/C@Bi_2MoO_6$ composite.

The Br^- concentration in the degradation process was detected at different time intervals, as shown in Fig. 6b. The Br^- concentration in the degradation solution keeps increasing with the visible-light irradiation time over the $C@Bi_2MoO_6$ and $Ag/C@Bi_2MoO_6$ composites, indicating a continuous debromination during the 2,4-DBP degradation. The debromination rate of 0.5% $Ag/C@Bi_2MoO_6$ composite is 2.8 times than that of $C@Bi_2MoO_6$ without Ag deposition, suggesting that Ag deposition favors the debromination process of 2,4-DBP. Furthermore, the coated carbon layer and deposited Ag nanoparticles are very stable, and it is confirmed by the recycling test as shown in Fig. 6c. After four repeated degradation tests, the 2,4-DBP removal rates have no significant decrease, showing the practical application stability of the $Ag/C@Bi_2MoO_6$ composite.

As we know, degradation means any bond breaking in the structures of the compound. According to the results of removal and debromination rates, the 2,4-DBP removal almost synchronizes with the debromination process, suggesting that the debromination process is the major pathway for 2,4-DBP degradation. The photoexcited electrons

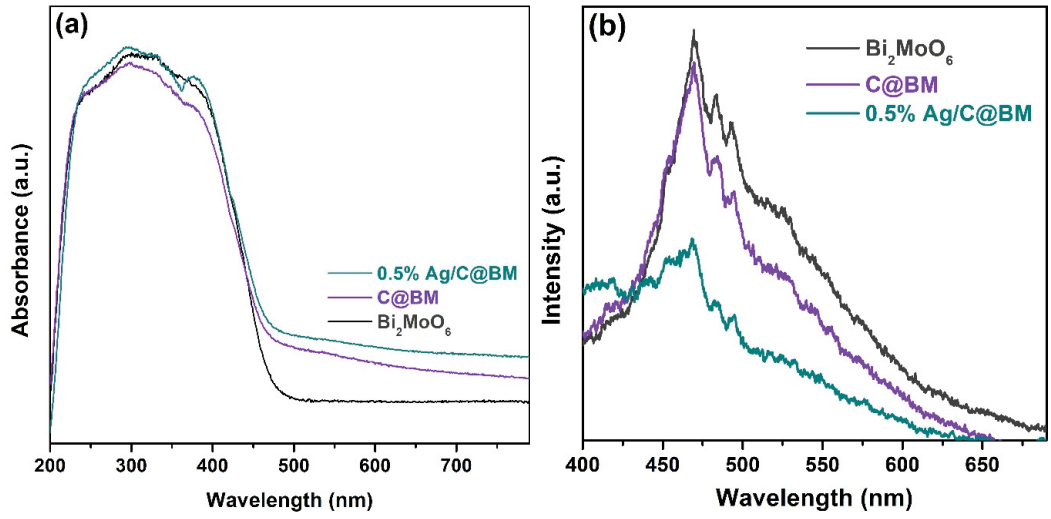

Fig. 5. (a) UV-Vis DRS curves and (b) PL spectra of the pure Bi_2MoO_6, $C@Bi_2MoO_6$ and 0.5% $Ag/C@Bi_2MoO_6$ (BM) composite.

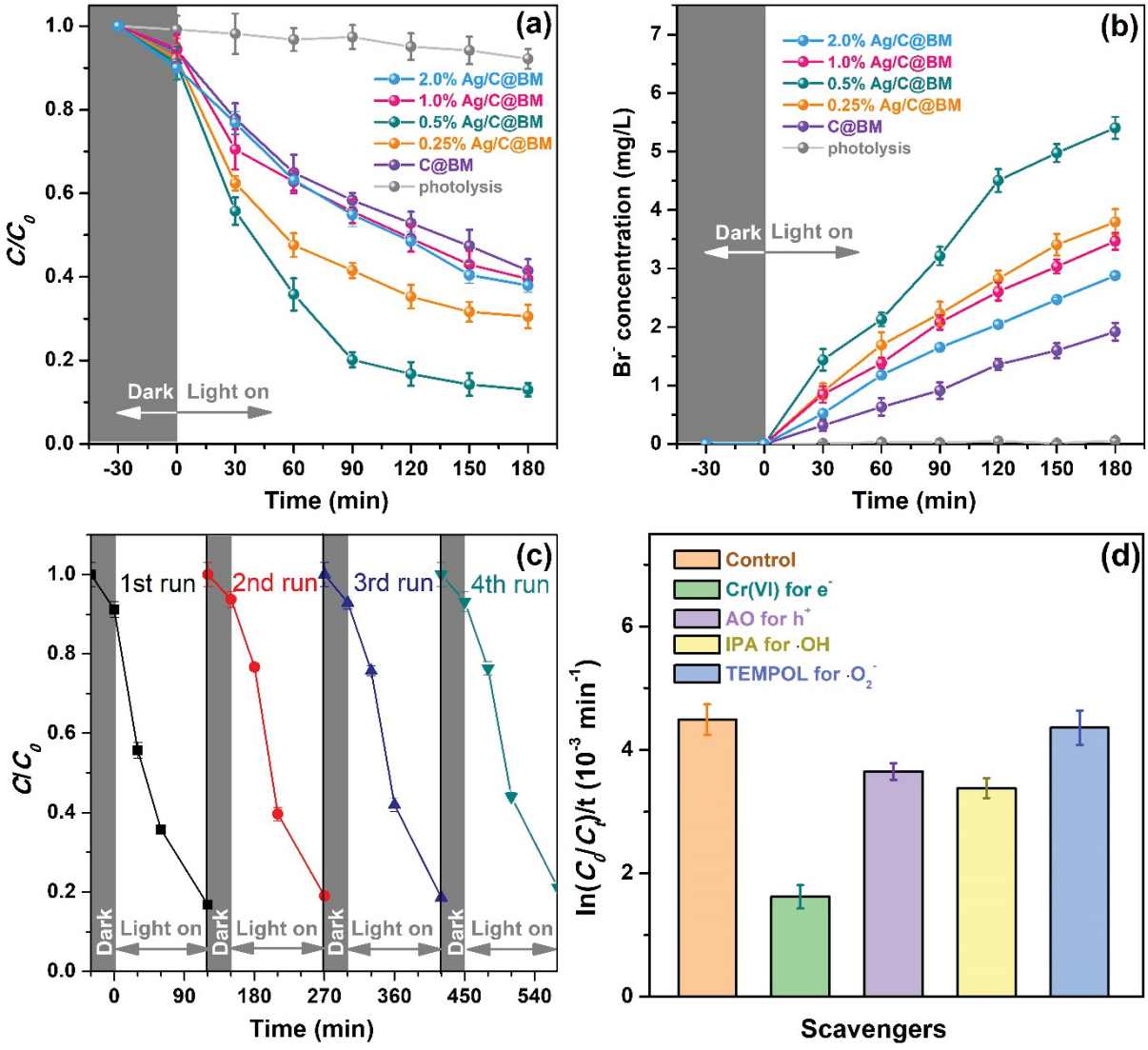

Fig. 6. (a) Photocatalytic degradation curves, (b) corresponding Br^- concentration during DBP degradation under visible light irradiation over the pure Bi_2MoO_6, $C@Bi_2MoO_6$ and $Ag/C@Bi_2MoO_6$ (BM) composites, (c) recycling tests of the 0.5% $Ag/C@Bi_2MoO_6$ composite under visible light irradiation by degradation of DBP, and (d) effects of different scavengers on DBP removal rate over the 0.5% $Ag/C@Bi_2MoO_6$ composite under visible light irradiation within for 120 min. The photocatalyst dosage is 1.0 g/L and DBP initial concentration is 10 mg/L.

and holes and the following active radicals, such as •OH and $•O_2^-$, would be likely to contribute to the debromination and degradation process of 2,4-DBP [35]. To reveal the roles of photoexcited radicals, scavenger detecting was used in this study and the results are shown in Fig. 6c. The capture of $•O_2^-$ radical has no obvious change on 2,4-DBP removal rates, demonstrating that the $•O_2^-$ is an invalid radical for 2,4-DBP degradation. When we scavenge the holes and the following •OH radicals, the 2,4-DBP removal rates slightly decrease, indicating that the radicals do not play major parts in the photocatalytic process over the 0.5% $Ag/C@Bi_2MoO_6$ composite. However, the 2,4-DBP removal rate is remarkably inhibited due to the photoexcited electrons captured. It suggests that the electronic pathway is dominant within 2,4-DBP removal and the photoexcited electrons play very significant roles in the 2,4-DBP debromination process.

Bi_2MoO_6 is a visible-light generated semiconductor and it has a narrow bandgap with the E_g of 2.2 eV. In the previous work, we have measured the positions of the conduction band (CB) and valence band (VB), and they are +1.0 and +3.2 eV, respectively [33,36]. As shown in Fig. 7, the potential of CB is higher than that of $O_2/•O_2^-$, thus the $•O_2^-$ radical would not be generated in CB of Bi_2MoO_6. It is consistent with the scavenger results in Fig. 6d. The photoexcited electrons and holes are separated on the surface of the $Ag/C@Bi_2MoO_6$ composite under the visible-light irradiation and the carbon layer could accelerate the electron transmission to the surface of the composite. At the same time, the electric field would be generated by the plasmonic effect of Ag^0 atoms and aggregate much more electrons around the Ag^0 atoms [37,38]. The photoexcited electrons have a strongly reductive activity

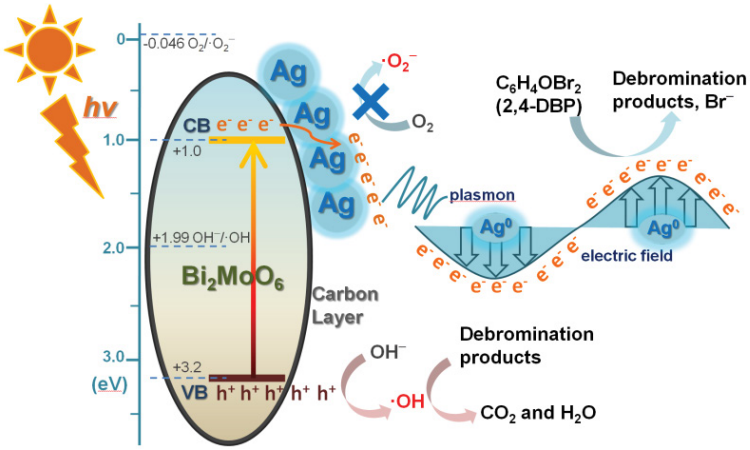

Fig. 7. Possible mechanism of photocatalytic degradation of 2,4-DBP over the Ag/C@Bi_2MoO_6 composite under visible light irradiation.

to break the C–Br bond in 2,4-DBP structure and they act as the major radicals in the 2,4-DBP debromination process. As the following step, the debromination products would be decomposed and mineralized by the •OH radicals generated from the photoexcited holes.

4. Conclusions

The Ag/C@Bi_2MoO_6 composite photocatalyst was prepared by two steps with hydrothermal and ultrasonic deposition methods. The 0.5% Ag/C@Bi_2MoO_6 composite was proved to be more efficient and reliable in 2,4-DBP photocatalytic degradation under visible-light irradiation. The hydrothermal carbon layer provides a rapid transmission route by its excellent conductivity to enhance the separation of photoexcited charges and the Ag nanoparticles could build an electric field to aggregate much more electrons to reduce the contaminant. The degradation of 2,4-DBP is launched with debromination process in the conduction band by aggregating electrons, and the following oxidization process in valence band would completely mineralize 2,4-DBP by holes and •OH radicals. The result provides new insight into halophenols degradation by the photocatalytic process.

Acknowledgments

This work was supported by the National Natural Science Foundation of China (No. 51678323), the Key Research and Development Program of Shandong Province (No. 2019GSF109048), the Project of Shandong Province Higher Educational Science and Technology Program (No. J17KA110).

References

[1] Q. Zhang, W. Kong, L. Wei, Y. Wang, Y. Luo, P. Wang, J. Liu, J.L. Schnoor, G. Jiang, Uptake, phytovolatilization, and interconversion of 2,4-dibromophenol and 2,4-dibromoanisole in rice plants, Environ. Int., 142 (2020) 105888, doi: 10.1016/j.envint.2020.105888.

[2] D. Ma, J. Wu, M.C. Gao, Y.J. Xin, C. Chai, Enhanced debromination and degradation of 2,4-dibromophenol by an Z-scheme Bi_2MoO_6/CNTs/g-C_3N_4 visible light photocatalyst, Chem. Eng. J., 316 (2017) 461–470.

[3] S.O. Ganiyu, E.D. van Hullebusch, M. Cretin, G. Esposito, M.A. Oturan, Coupling of membrane filtration and advanced oxidation processes for removal of pharmaceutical residues: a critical review, Sep. Purif. Technol., 156 (2015) 891–914.

[4] F.C. Moreira, R.A.R. Boaventura, E. Brillas, V.J.P. Vilar, Electrochemical advanced oxidation processes: A review on their application to synthetic and real wastewaters, Appl. Catal., B, 202 (2017) 217–261.

[5] R. Asahi, T. Morikawa, T. Ohwaki, K. Aoki, Y. Taga, Visible-light photocatalysis in nitrogen-doped titanium oxides, Science, 293 (2001) 269–271.

[6] D. Ma, Y.J. Xin, M.C. Gao, J. Wu, Fabrication and photocatalytic properties of cationic and anionic S-doped TiO_2 nanofibers by electrospinning, Appl. Catal., B, 147 (2014) 49–57.

[7] S. Dolatabadia, M. Fattahi, M. Nabatib, Solid state dispersion and hydrothermal synthesis, characterization and evaluations of TiO_2/ZnO nanostructures for degradation of Rhodamine B, Desal. Water Treat., 231 (2021) 425–435.

[8] A. Akhundi, A. Badiei, G.M. Ziarani, A. Habibi-Yangjeh, M.J. Muñoz-Batista, R. Luque, Graphitic carbon nitride-based photocatalysts: toward efficient organic transformation for value-added chemicals production, Mol. Catal., 488 (2020) 110902, doi: 10.1016/j.mcat.2020.110902.

[9] Y. Zheng, T.F. Zhou, X.D. Zhao, W.K. Pang, H. Gao, S. Li, Z. Zhou, H.K. Liu, Z.P. Guo, Atomic interface engineering and electric-field effect in ultrathin Bi_2MoO_6 nanosheets for superior lithium ion storage, Adv. Mater., 29 (2017) 1700396, doi: 10.1002/adma.201700396.

[10] D.M. Chen, Q. Hao, Z.H. Wang, H. Ding, Y.F. Zhu, Influence of phase structure and morphology on photocatalytic activity of bismuth molybdates, CrystEngComm, 18 (2016) 1976–1986.

[11] F.E. Osterloh, Inorganic nanostructures for photoelectrochemical and photocatalytic water splitting, Chem. Soc. Rev., 42 (2012) 2294–2320.

[12] X. Xu, L. Meng, Y. Dai, M. Zhang, C. Sun, S. Yang, H. He, S. Wang, H. Li, Bi spheres SPR-coupled Cu_2O/Bi_2MoO_6 with hollow spheres forming Z-scheme Cu_2O/Bi/Bi_2MoO_6 heterostructure for simultaneous photocatalytic decontamination of sulfadiazine and Ni(II), J. Hazard. Mater., 381 (2020) 120953, doi: 10.1016/j.jhazmat.2019.120953.

[13] Q. Hao, R.T. Wang, H.J. Lu, C.A. Xie, W.H. Ao, D.M. Chen, C. Ma, W.Q. Yao, Y.F. Zhu, One-pot synthesis of C/Bi/Bi_2O_3 composite with enhanced photocatalytic activity, Appl. Catal., B, 219 (2017) 63–72.

[14] J.H. Bi, W. Fang, L. Li, X.F. Li, M.H. Liu, S.J. Liang, Z.Z. Zhang, Y.H. He, H.X. Lin, L. Wu, S.W. Liu, P.K. Wong, Ternary reduced-graphene-oxide/Bi_2MoO_6/Au nanocomposites with enhanced photocatalytic activity under visible light, J. Alloys Compd., 649 (2015) 28–34.
[15] Z.X. Chen, Y. Wu, J.J. Xu, F.X. Wang, J. Wang, J.Y. Zhang, Z.Y. Ren, Y.H. He, G.C. Xiao, Synthesis of C-coated $ZnIn_2S_4$ nanocomposites with enhanced visible light photocatalytic selective oxidation activity, J. Mol. Catal. A: Chem., 401 (2015) 66–72.
[16] Y.Y. Sun, J. Wu, T.J. Ma, P.C. Wang, C.Y. Cui, D. Ma, Synthesis of C@Bi_2MoO_6 nanocomposites with enhanced visible light photocatalytic activity, Appl. Surf. Sci., 403 (2017) 141–150.
[17] T.J. Ma, J. Wu, Y.D. Mi, Q.H. Chen, D. Ma, C. Chai, Novel Z-scheme g-C_3N_4/C@Bi_2MoO_6 composite with enhanced visible-light photocatalytic activity for β-naphthol degradation, Sep. Purif. Technol., 183 (2017) 54–65.
[18] M. Murdoch, G.I.N. Waterhouse, M.A. Nadeem, J.B. Metson, M.A. Keane, R.F. Howe, J. Llorca, H. Idriss, The effect of gold loading and particle size on photocatalytic hydrogen production from ethanol over Au/TiO_2 nanoparticles, Nat. Chem., 3 (2011) 489–492.
[19] J. Wu, Y.X. Zhang, T. Wang, Y.J. Xin, D. Ma, Au nanoparticles and graphene oxide co-loaded graphitic carbon nitride: synthesis and photocatalytic application, Mater. Res. Bull., 100 (2018) 282–288.
[20] W.J. Liao, Y.R. Zhang, M. Zhang, M. Murugananthan, S. Yoshihara, Photoelectrocatalytic degradation of microcystin-LR using Ag/AgCl/TiO_2 nanotube arrays electrode under visible light irradiation, Chem. Eng. J., 231 (2013) 455–463.
[21] P. Chowdhury, G. Malekshoar, M.B. Ray, J. Zhu, A.K. Ray, Sacrificial hydrogen generation from formaldehyde with Pd/TiO_2 photocatalyst in solar radiation, Ind. Eng. Chem. Res., 52 (2013) 5023–5029.
[22] A. Meng, L. Zhang, B. Cheng, J. Yu, TiO_2-MnO_x-Pt hybrid multiheterojunction film photocatalyst with enhanced photocatalytic CO_2-reduction activity, ACS Appl. Mater. Interfaces, 11 (2018) 5581–5589.
[23] Y.X. Zhang, J. Wu, Y.Y. Deng, Y.J. Xin, H.L. Liu, D. Ma, N. Bao, Synthesis and visible-light photocatalytic property of Ag/GO/g-C_3N_4 ternary composite, Mater. Sci. Eng. B, 221 (2017) 1–9.
[24] P. Panchal, D.R. Paul, A. Sharma, P. Choudhary, P. Meena, S.P. Nehra, Biogenic mediated Ag/ZnO nanocomposites for photocatalytic and antibacterial activities towards disinfection of water, J. Colloid Interface Sci., 563 (2020) 370–380.
[25] Y.J. Chen, G.H. Tian, Y.H. Shi, Y.T. Xiao, H.G. Fu, Hierarchical MoS_2/Bi_2MoO_6 composites with synergistic effect for enhanced visible photocatalytic activity, Appl. Catal., B, 164 (2015) 40–47.
[26] J. Di, J.X. Xia, M.X. Ji, H.P. Li, H. Xu, H.M. Li, R. Chen, The synergistic role of carbon quantum dots for the improved photocatalytic performance of Bi_2MoO_6, Nanoscale, 7 (2015) 11433–11443.
[27] Y.H. Chiu, Y.J. Hsu, Au@Cu_2S_4 yolk@shell nanocrystal-decorated TiO_2 nanowires as an all-day-active photocatalyst for environmental purification, Nano Energy, 31 (2017) 286–295.
[28] R. Sellappan, M.G. Nielsen, F. Gonzalez-Posada, P.C.K. Vesborg, I. Chorkendorff, D. Chakarov, Effects of plasmon excitation on photocatalytic activity of Ag/TiO_2 and Au/TiO_2 nanocomposites, J. Catal., 307 (2013) 214–221.
[29] H.P. Li, W.G. Hou, X.T. Tao, N. Du, Conjugated polyene-modified Bi_2MO_6, (M, Mo or W) for enhancing visible light photocatalytic activity, Appl. Catal. B, 172–173 (2015) 27–36.
[30] S.D. Gardner, C.S.K. Singamsetty, G.L. Booth, G.R. He, C.U.P. Jr, Surface characterization of carbon fibers using angle-resolved XPS and ISS, Carbon, 33 (1995) 587–595.
[31] L.Q. Ye, J.Y. Liu, C.Q. Gong, L.H. Tian, T.Y. Peng, L. Zan, Two different roles of metallic Ag on Ag/AgX/BiOX (X = Cl, Br) visible light photocatalysts: surface plasmon resonance and Z-scheme bridge, ACS Catal., 2 (2012) 1677–1683.
[32] W. Chen, G.R. Duan, T.Y. Liu, Fabrication of Bi_2MoO_6, nanoplates hybridized with g-C_3N_4, nanosheets as highly efficient visible light responsive heterojunction photocatalysts for Rhodamine B degradation, Mater. Sci. Semicond. Process., 35 (2015) 45–54.
[33] D. Ma, J. Wu, M.C. Gao, Y.J. Xin, T.J. Ma, Y.Y. Sun, Fabrication of Z-scheme g-C_3N_4/RGO/Bi_2WO_6 photocatalyst with enhanced visible-light photocatalytic activity, Chem. Eng. J., 290 (2016) 136–146.
[34] J. Yang, S.H. Cui, J.Q. Qiao, H.Z. Lian, The photocatalytic dehalogenation of chlorophenols and bromophenols by cobalt doped nano TiO_2, J. Mol. Catal. A, 395 (2014) 42–51.
[35] Q.Q. Li, G.J. Su, M.H. Zheng, M.J. Wang, Y.L. Liu, F. Luo, Y.Y. Gu, R. Jin, Thermal oxidation degradation of 2,2′,4,4′-tetrabromodiphenyl ether over Li_xTiO_x micro/nanostructures with dozens of oxidative product analyses and reaction mechanisms, Environ. Sci. Technol., 51 (2017) 10059–10071.
[36] D. Ma, J. Wu, M.C. Gao, Y.J. Xin, Y.Y. Sun, T.J. Ma, Hydrothermal synthesis of an artificial Z-scheme visible light photocatalytic system using reduced graphene oxide as the electron mediator, Chem. Eng. J., 313 (2017) 1567–1576.
[37] C.C. Nguyen, D.T. Nguyen, T.O. Do, A novel route to synthesize C/Pt/TiO_2 phase tunable anatase-rutile TiO_2 for efficient sunlight-driven photocatalytic applications, Appl. Catal., B, 226 (2018) 46–52.
[38] V. Sharma, S. Kumar, V. Krishnan, Homogeneously embedded Pt nanoclusters on amorphous titania matrix as highly efficient visible light active photocatalyst material, Mater. Chem. Phys., 179 (2016) 129–136.